

Highlights

Disentangling Slow and Fast Temporal Dynamics in Degradation Inference with Hierarchical Differential Models

Mengjie Zhao, Olga Fink

- Learned latent states align well with true physical degradation.
- The framework shows robust generalization to unseen conditions.
- The primary latent component serves as an interpretable health indicator.
- H-CDE effectively models degradation across diverse system dynamics.

Disentangling Slow and Fast Temporal Dynamics in Degradation Inference with Hierarchical Differential Models

Mengjie Zhao, Olga Fink

Swiss Federal Institute of Technology Lausanne (EPFL), Switzerland

Abstract

Reliable inference of system degradation from sensor data is fundamental to condition monitoring and prognostics in engineered systems. Since degradation is rarely observable and measurable, it must be inferred to enable accurate health assessment and decision-making. This is particularly challenging because operational and environmental variations dominate system behavior, while degradation introduces only subtle, long-term changes. Consequently, sensor data primarily reflect short-term operational variability, making it difficult to disentangle the underlying degradation process. Residual-based methods are widely employed, but the residuals remain entangled with operational history, often resulting in noisy and unreliable degradation estimation, particularly in systems with dynamic responses. Other approaches often focus on modeling degradation-aware degradation dynamics but overlook how operational history drives long-term degradation. Neural Ordinary Equations (NODEs) offer a promising framework for inferring latent dynamics, but the time-scale separation in slow-fast systems introduces numerical stiffness and complicates training, while degradation disentanglement remains difficult. To address these limitations, we propose a novel Hierarchical Controlled Differential Equation (H-CDE) framework that incorporates a slow (degradation) and a fast (operation) CDE component in a unified architecture. It introduces three key innovations: a multi-scale time integration scheme to mitigate numerical stiffness; a learnable path transformation that extracts latent degradation drivers to control degradation evolution; and a

Email addresses: `mengjie.zhao@epfl.ch` (Mengjie Zhao), `olga.fink@epfl.ch` (Olga Fink)

novel activation function that enforces monotonicity on inferred degradation as a regularizer for disentanglement. Through comprehensive evaluations on both dynamic response (e.g., bridges) and steady state (e.g., aero-engine) systems, we demonstrate that H-CDE effectively disentangles degradation from operational dynamics and outperforms residual-based baselines, yielding more accurate, robust, and interpretable inference.

Keywords: Neural ODE, Neural CDE, Degradation Inference, Slow-Fast Systems, Multi-Scale Dynamics, Hierarchical Models, Disentanglement, Prognostics, Structural Health Monitoring, Degradation Modeling, Condition Monitoring, Health Index

1. Introduction

Ensuring the reliability and safety of complex engineered systems, ranging from critical infrastructure [1] to industrial machinery [2] and aerospace structures [3], relies on continuous monitoring of their health state. A key indicator of system health is the level of degradation, whose progression enables estimation of the remaining useful life (RUL). Accurate RUL predictions support predictive maintenance strategies and help avoid both unexpected failures and unnecessarily conservative component replacements [4, 5]. However, degradation is rarely directly measurable and often needs to be inferred from sensor data. This is particularly challenging because sensor responses are dominated by operational and environmental variations, while degradation introduces only subtle, long-term changes in system behavior. Disentangling these subtle degradation effects from dominant operational variations makes accurate inference a difficult task.

Current approaches to degradation inference typically focus on either modeling the degradation process itself or capturing degradation-aware system dynamics [6, 7]. *Reliability-based* methods model the macroscopic progression of degradation as stochastic processes. Common choices include Gamma processes, Wiener processes with drift, and Weibull-type accelerated life models [8]. These models often assume that degradation evolves independently of external factors or incorporate such influences in a simplified, parametric form [6]. While effective in certain applications, they rely on strong distributional assumptions and lack flexibility in adapting to changing operating conditions [9]. A second family of methods aims to infer degradation by modeling how it affects system dynamics under different operating condi-

tions. This requires knowledge, or an approximation, of the system’s healthy behavior. When the underlying physics is known or partially known, *physics-based* models can be employed. These models incorporate prior knowledge of the underlying dynamics, and the hidden degradation state can be inferred from sensor measurements using filtering techniques such as Kalman filters [10] or particle filters [11]. However, in many real-world systems, the governing physics is unknown or too complex to model accurately. In such cases, *data-driven* methods are increasingly favored for their ability to learn both the system dynamics and the latent degradation state directly from observed data [12].

One common data-driven degradation inference method is residual-based modeling, widely adopted for its simplicity. It learns a representation of system behavior under healthy conditions and interprets deviations from this baseline as indicators of degradation [13, 14]. However, the inferred degradation is often noisy, as these methods assume that measured states from the degraded system can be expressed as a linear combination of nominal response and degradation effects. In practice, the impact of degradation on system behavior is highly nonlinear [15]. These unmodeled nonlinear dependencies lead to discrepancies that remain entangled with the operating history, making it difficult to isolate the true degradation. To address this, more recent methods model degradation-aware operational dynamics by explicitly conditioning system behavior on the inferred degradation state. These approaches typically learn a mapping from control inputs, external factors, and the latent degradation state to sensor measurements, while enforcing that the latent state meaningfully represents actual degradation. One common strategy is to incorporate prior knowledge, such as monotonicity and trendability, directly into the loss function [16]. Other approaches introduce inductive biases at the model level, for instance by modeling the degradation progression using a Koopman operator [17]. While these methods capture how degradation affects system responses, they do not explicitly model how operational history contributes to degradation progression. As a result, they may generalize poorly to new units operated under different conditions, leading to overestimation or underestimation of degradation under novel conditions.

In addition, degradation manifests differently across engineering domains. For high-cycle components or subsystems such as batteries [18], aero-engines [19], or gearboxes [20], the system dynamics are often assumed to reach equilibrium at each operating point. In these *steady-state systems*, degradation primarily affects efficiency and can be modeled as an additional input influ-

encing the mapping from control inputs and external conditions to sensor measurements [21]. Most existing data-driven degradation inference methods are designed for this type of system. In contrast, infrastructure systems such as bridges or wind turbines experience dynamic loading and continuous response. In these systems, degradation, typically caused by material deterioration such as stiffness loss due to cracks or corrosion [7], interacts nonlinearly with the system’s transient behavior [1]. We refer to these systems as *dynamic-response systems*. For such systems, residual-based methods struggle to isolate degradation due to the nonlinear entanglement between degradation and operational dynamics. Approaches that attempt to model system behavior conditioned on degradation must also learn accurate dynamic models from condition monitoring data, which is inherently difficult. Moreover, it is challenging to ensure that the inferred latent variables truly represent degradation, especially in the absence of direct supervision or knowledge of the underlying physics [22].

To accurately disentangle degradation from operational dynamics, a strong inductive bias is essential. In many practical scenarios, the underlying physical model is unknown, and the only available prior knowledge is that degradation progresses monotonically over time and that its rate of change depends on the operational history. To incorporate this structure, we propose a method that jointly models both the operational dynamics conditioned on degradation and the degradation progression driven by system usage. We propose to infer the degradation state through a progression model constrained to be monotonically increasing and use it as a latent variable to guide the learning of operational dynamics. By modeling these two processes simultaneously, the degradation dynamics act as a regularizer and provides a strong inductive bias for learning complex, transient system behavior. This coupling enables the model to capture nonlinear dynamic responses while isolating a physically meaningful latent degradation representation.

To achieve this, we first need to infer the underlying system dynamics from condition monitoring data. Neural Ordinary Differential Equations (NODEs) offer a promising framework by parameterizing continuous-time dynamics using neural networks [23]. This yields smooth latent trajectories, which are well-suited for capturing long-range temporal dependencies. However, standard NODEs are limited in their ability to model systems influenced by control inputs or external factors. Since their dynamics are defined solely by the initial condition, the system’s evolution during inference remains fixed and cannot adapt to changes in external inputs over time. Neural Controlled

Differential Equations (NCDEs) [24] overcome this limitation by treating the input data stream as a control signal that drives the system. This enables NCDEs to incorporate the full operational history and evolve dynamically in response to changing conditions.

However, degrading systems introduce additional complexity because they exhibit multiscale dynamics, with degradation progressing much more slowly than operational dynamics. While NCDEs effectively model controlled continuous-time systems, they are primarily designed for single-timescale behavior. When applied to multiscale systems, standard NODE-based models (including NCDEs) suffer from numerical stiffness due to the large disparity in time scales between fast and slow processes. Mitigating this stiffness requires extremely small integration steps, which significantly increases computational cost and may even prevent the model from learning altogether [25, 26].

To address these challenges, we propose the Hierarchical Controlled Differential Equation (H-CDE) framework for disentangled degradation inference. H-CDE disentangles slow degradation dynamics from fast operational fluctuations through a two-layer hierarchical structure: a high-level module learns long-term degradation progression, while a lower-level module captures short-term operational dynamics conditioned on the inferred degradation state. To mitigate numerical stiffness, H-CDE adopts a multi-scale integration scheme, using coarse integration steps for the slow dynamics and finer steps for the fast dynamics. To prevent contamination of the slow degradation process by high-frequency operational noise, a learnable transformation extracts latent degradation drivers aligned with the degradation timescale in the slow layer. Finally, we enforce monotonic degradation progression through a custom activation function in the differential operator, which acts as a regularizer for disentanglement.

We evaluate H-CDE on two different case studies: a bridge structure with *dynamic-response* and a turbofan engine operating under quasi-steady conditions. These case studies demonstrate the framework’s broad applicability in disentangling latent degradation states across systems with fundamentally different dynamical behavior. To the best of our knowledge, this is the first study to compare degradation inference across such fundamentally different dynamical regimes, whereas prior work has primarily focused on steady-state systems. Our contributions include:

- Simultaneously inferring degradation-aware operational dynamics and degradation progression driven by system usage.

- Capturing long-range temporal dependencies in degradation through a multiscale integration scheme tailored to fast and slow dynamics.
- Enforcing monotonic degradation progression via a custom differential operator, which acts as an effective regularizer for disentanglement.

The remainder of the paper is organized as follows. Section 2 reviews related work. Section 3 introduces the necessary preliminaries. The proposed H-CDE framework is presented in Section 4. Section 5 describes the case studies, followed by the experimental setup in Section 6. Results and discussions are provided in Section 7, and conclusions along with future directions are presented in Section 8.

2. Related Works

This section first reviews prior works on data-driven degradation inference methods. Since our framework builds on Neural CDEs, we then dedicate a separate subsection to NODE-based methods for latent dynamics learning, with a focus on long-range dependencies and multi-scale dynamics, both crucial for degradation inference.

2.1. Data-Driven Degradation Inference

Degradation inference and subsequent Health Indicator (HI) construction from unlabeled sensor data are essential tasks in Prognostics and Health Management (PHM) [27]. Both aim to uncover the underlying degradation states (potentially multi-dimensional), while HI construction derives a scalar trajectory (normalized to $[0, 1]$) for health tracking and RUL prediction, typically requiring run-to-failure trajectories for training. The central challenge for both tasks is disentangling latent degradation states from noise and operational variations. Thus, we review methods addressing both degradation inference and HI construction.

Snapshot-based modeling. These methods learn the system’s behavior at discrete time points. A common approach is residual-based modeling, where the system is trained only on healthy data to capture normal behavior. At test time, deviations from these learned behaviors, i.e., the residuals, are treated as degradation indicators from which HI can be derived. And learning this healthy system behavior can be done either by mapping operating conditions to outputs [14], or by using Autoencoders (AEs) and

Variational Autoencoders (VAEs), where the residual corresponds to the reconstruction error [28]. The resulting residuals can then be aggregated into a scalar health indicator, for instance, through dimensionality reduction methods [13]. While such approaches have practical utility, they are primarily designed to reproduce healthy behavior rather than model degradation progression; therefore do not fulfill important criteria such as monotonicity and disentanglement of degradation from operational variations.

Regularization and constraints. To address these limitations, some methods incorporate domain knowledge or physical principles through constraints. Examples include monotonicity and trendability constraints in Autoencoders [16], trend constraints in VAEs [29], and semi-supervised approaches with isotonic projections ensuring monotonicity [30].

Sequence-based modeling. Sequence models explicitly model degradation-aware operational dynamics. For instance, Garmaev et al. [17] apply Koopman operators within deep networks, using operating conditions as additional inputs to reconstruct degradation-aware dynamics. Moving towards attention mechanisms, Biggio et al. [31] use Transformer encoders to embed ageing states from short voltage/current windows and condition Transformer decoders to reconstruct full discharge curves. Bridging discrete and continuous approaches, Pepe et al. [32] combine augmented Neural ODEs with predictor-corrector RNNs to forecast cycle-level state of health and end-of-life. Similarly, Zhou et al. [33] embed discretized Neural ODEs within a Dynamic Governing Network, driven by time-varying coefficients to estimate smooth RUL trajectories. While these methods effectively incorporate inferred degradation states into operating dynamics modeling, they often neglect how long-term operational histories drive degradation and lack mechanisms to impose regularization or physical constraints on its progression. Consequently, they are expected to generalize poorly to unseen operational patterns. Moreover, most applications focus on steady state systems such as batteries or aero-engines, with limited attention to dynamic response systems such as those in structural health monitoring [7].

2.2. Neural Ordinary Differential Equations (NODEs)

NODEs [34, 35] and their extension, Neural Controlled Differential Equations (NCDEs) [24], gained popularity in dynamics modeling as they capture system evolution directly in continuous time, providing a principled way to handle irregular sampling and generate smooth trajectories.

Long-range temporal dependencies. Early implementations often faced difficulties with long-range dependencies due to training instability, but recent advances have improved performance. For instance, rough-path CDEs use log-signatures as statistics to describe how the signal drives the CDE and improve memory over long horizons [36], Neural Laplace models dynamics in the Laplace domain for more efficient, long-term prediction [37], and integrating accelerated optimization schemes like Nesterov method with adaptive solvers markedly enhances convergence and stability during training [38].

Multiscale dynamics modeling NODEs are rarely applied to multi-scale systems, as they often suffer from stiffness caused by scale separation. While limited efforts focus specifically on mitigating these issues, for example, by developing multi-scale integration schemes [39] or employing hierarchical NODEs tailored to distinct predefined timescales (e.g., minute vs. hour) [40], such approaches still struggle to disentangle slow and fast components effectively. A further limitation lies in handling varying operating conditions. While CDEs enable control via observed inputs, directly using raw sensor paths introduces timescale mismatch and noise, hindering disentanglement. As a result, existing methods rarely address the combined challenge of dynamic operating conditions, multi-scale dynamics, and latent disentanglement within a unified framework.

3. Preliminaries

Many real-world processes, including the operation and degradation of industrial and infrastructure assets, evolve continuously over time and depend on both internal state and external inputs. To capture such behavior, this section introduces two foundational frameworks for learning continuous-time dynamics: Neural Ordinary Differential Equations (NODEs) and their extension, Neural Controlled Differential Equations (NCDEs).

3.1. Neural ODEs

Neural Ordinary Differential Equations (NODEs) [34] provide a framework for modeling the continuous evolution of a hidden state $\mathbf{z}(t) \in \mathbb{R}^d$. The core idea is to parameterize the time derivative of the state using a neural network $f_\theta : \mathbb{R}^d \times \mathbb{R} \rightarrow \mathbb{R}^d$ with parameters θ :

$$\frac{d\mathbf{z}(t)}{dt} = f_\theta(\mathbf{z}(t), t). \quad (1)$$

Given an initial state \mathbf{z}_0 at time t_0 , the trajectory $\mathbf{z}(t)$ for $t > t_0$ is obtained by solving this ordinary differential equation (ODE). NODEs are particularly well-suited for modeling autonomous systems where the dynamics explicitly depend only on the current state and time. However, this means that once f is learned, the solution of NODE is determined by the initial condition \mathbf{z}_0 ; there is no direct mechanism to incorporate data that arrives after the initial time point. To address this limitation, Neural Controlled Differential Equations (NCDEs) [24] provide a more flexible framework that naturally adjusts the trajectory based on subsequent observations.

3.2. Neural CDEs

Neural Controlled Differential Equations (NCDEs) [24] provide a framework for modeling the continuous-time evolution of a hidden state $\mathbf{z}(t) \in \mathbb{R}^d$ as it responds to a continuous control path $\mathbf{X}(t) \in \mathbb{R}^m$. The dynamics are defined by the controlled differential equation:

$$d\mathbf{z}(t) = f_\theta(\mathbf{z}(t))d\mathbf{X}(t). \quad (2)$$

Here, $f_\theta : \mathbb{R}^d \rightarrow \mathbb{R}^{d \times m}$ is a neural network, parameterized by θ , mapping the current state $\mathbf{z}(t)$ to a matrix. The term $f_\theta(\mathbf{z}(t))d\mathbf{X}(t)$ represents matrix-vector multiplication, determining the infinitesimal change in the state in response to an infinitesimal change in the control path. Integrating Eq. (2) over a time interval $[t_0, t]$ gives the state's trajectory:

$$\mathbf{z}(t) = \mathbf{z}(t_0) + \int_{t_0}^t f_\theta(\mathbf{z}(s))d\mathbf{X}(s). \quad (3)$$

This integral is a Riemann-Stieltjes integral, and allows the hidden state $\mathbf{z}(t)$ to evolve in response to the trajectory of the driving signal $\mathbf{X}(t)$.

Assuming the observed discrete time series $\mathbf{x} = \{(t_0, \mathbf{x}_0), \dots, (t_N, \mathbf{x}_N)\}$ (with $\mathbf{x}_i \in \mathbb{R}^n$) is a discretization of an underlying continuous process $\mathbf{X}(t)$, we can then approximate $\mathbf{X}(t)$ by interpolating the observations \mathbf{x} , for instance, using natural cubic splines [24]. This yields a smooth path $\mathbf{X}(t) : [t_0, t_N] \rightarrow \mathbb{R}^m$ satisfying $\mathbf{X}(t_i) = (\mathbf{x}_i, t_i)$, where time is appended as an additional channel ($m = n + 1$). The differentiability of this interpolated path allows the CDE (Eq. (2)) to be expressed as an equivalent ODE:

$$\frac{d\mathbf{z}(t)}{dt} = f_\theta(\mathbf{z}(t)) \frac{d\mathbf{X}(t)}{dt}, \quad (4)$$

which directly expresses the rate of change of the latent state as a function of the rate of change of the driving signal.

While this formulation is well-suited for modeling dynamics driven by a single control path, standard NCDEs do not inherently account for coupled dynamics across distinct time scales, such as the multi-scale behavior often found in degradation processes.

4. Problem Formulation and Proposed Framework

4.1. System Dynamics and Degradation Inference

Following the formulation in Zagorowska et al. [6], we model degraded systems as a coupled slow-fast dynamical system with two coupled processes: (1) the progression of degradation driven by historical usage, and (2) the operating dynamics that are degradation-aware:

$$\begin{aligned}\frac{d\mathbf{d}(t)}{dt} &= \epsilon g(\mathbf{x}(t), \mathbf{u}(t), \mathbf{d}(t)), \\ \frac{d\mathbf{x}(t)}{dt} &= f(\mathbf{x}(t), \mathbf{u}(t), \mathbf{d}(t)).\end{aligned}\tag{5}$$

Here, $\mathbf{d}(t) \in \mathbb{R}^m$ denotes the slow degradation state, $\mathbf{x}(t) \in \mathbb{R}^n$ the fast operational states, and $\mathbf{u}(t) \in \mathbb{R}^p$ the control inputs. The function $g(\cdot)$ models degradation accumulation, while $f(\cdot)$ governs immediate system behavior. The small perturbation parameter $0 < \epsilon \ll 1$ enforces a separation of time scales, with degradation evolving slowly at $O(1/\epsilon)$ compared to $O(1)$ for fast operational dynamics. This formulation captures how $\mathbf{d}(t)$ reflects long-term effects under rapidly changing operating conditions.

Within this framework, the degradation state $\mathbf{d}(t)$ is the primary quantity of interest for health assessment and prognostics, but is typically unobservable. We therefore define the problem of **Degradation Inference**: estimating $\mathbf{d}(t)$ from discrete measurements of the observable fast states $\mathbf{x}(t)$ and control inputs $\mathbf{u}(t)$.

4.2. Hierarchical Neural CDE Framework Overview

The slow-fast dynamic system in Eq. (5) provides the structural basis for modeling degradation, but the underlying functions f and g are unknown and must be learned from data. This is challenging because degraded systems are inherently *multiscale*, making it difficult to infer both latent dynamics

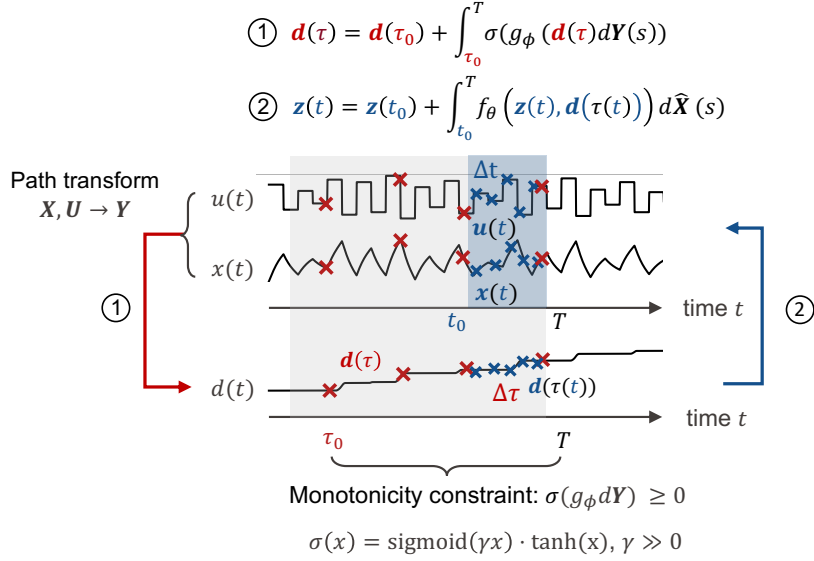


Figure 1: Overview of the Hierarchical CDE (H-CDE) framework designed for disentangling slow and fast dynamics. A hierarchy of CDEs models slow degradation and fast operations on distinct timescales (τ, t) , driven respectively by the slow degradation control path \mathbf{Y} (constructed via path transformation to derive degradation drivers) and the fast degradation-aware operational control path $\hat{\mathbf{X}}$. For slow CDE integrate over an extended horizon from τ_0 to T , while the fast CDE integrates over shorter periods from t_0 to T , with $\tau_0 < t_0$. A monotonicity constraint is enforced on the degradation dynamics through a novel activation function $\sigma(x)$.

and disentangle them. To address this, we propose the **Hierarchical Controlled Differential Equation (H-CDE)** framework, a hierarchical model based on NCDEs as introduced in Sec. 3.2. H-CDE is specifically designed to jointly infer and disentangle the coupled slow-fast dynamics. It employs two Neural CDEs to parameterize f_θ and g_ϕ , learning system dynamics from observations of $\mathbf{x}(t)$, $\mathbf{u}(t)$ while disentangling degradation states. The two Neural CDEs operate at different time scales: the slow CDE models long-term degradation at a coarser time resolution, while the fast CDE captures short-term operational dynamics at a finer time resolution, conditioned on the inferred degradation state. This hierarchical architecture separates slow degradation from fast fluctuations. To further enforce this separation, we

introduce a monotonicity regularizer that constrains the latent degradation state to evolve consistently over time. Since degradation is unobservable and only fast operational states are measured, we also apply a path transformation for the slow CDE to extract key degradation drivers and construct its control path.

An overview of the framework is shown in Fig. 1, which illustrates how the dynamics formulated in Eq. (5) are modeled within the H-CDE architecture. The remainder of this section elaborates its key components: Sec. 4.3 presents the **Multi-Scale Time Integration** scheme; Sec. 4.4 introduces the **Degradation Path Transformation** for constructing the slow degradation path $\mathbf{Y}(\tau)$; and Sec. 4.5 describes the **Monotonicity Constraint** enforced for degradation dynamics via a novel activation function.

4.3. Multi-Scale Time Integration

H-CDE aims to learn the underlying dynamics defined in Eqs. (5). However, learning such latent dynamics is challenging for Neural CDEs. Once the neural vector fields are parameterized, integrating and solving the coupled slow-fast system becomes difficult due to the stiffness from timescale separation [25]. This stiffness often enforces the use of prohibitively small integration steps or computationally expensive implicit solvers [26]. As a result, learning the neural vector fields end-to-end from data becomes particularly challenging.

To address this, we adopt the quasi-steady-state approximation [41], which exploits the inherent slowness of the degradation dynamics $\mathbf{d}(t)$ relative to the fast operational dynamics. This allows the slow trajectory to be computed independently and treated as quasi-static when solving for the fast dynamics, yielding the following decoupled integral forms:

$$\mathbf{d}(\tau) = \mathbf{d}(\tau_0) + \int_{\tau_0}^{\tau} g_{\phi}(\mathbf{d}(\tau)) d\mathbf{Y}(s) \quad \text{for } \tau \in (\tau_0, T], \quad (6)$$

$$\mathbf{z}(t) = \mathbf{z}(t_0) + \int_{t_0}^t f_{\theta}(\mathbf{z}(t), \mathbf{d}(\tau(t))) d\hat{\mathbf{X}}(s) \quad \text{for } t \in (t_0, T]. \quad (7)$$

Here, s denotes the integration variable. The initial states $\mathbf{d}(\tau_0)$ and $\mathbf{z}(t_0)$ are obtained from learned mappings: $\mathbf{d}(\tau_0) = \zeta_{\phi}(\mathbf{x}(\tau_0), \mathbf{u}(\tau_0), \tau_0)$ and $\mathbf{z}(t_0) = \xi_{\theta}(\mathbf{x}(t_0), \mathbf{u}(t_0), \mathbf{d}(t_0), t_0)$, where $\zeta_{\phi} : \mathbb{R}^{n+p+1} \rightarrow \mathbb{R}^m$ and $\xi_{\theta} : \mathbb{R}^{n+p+m+1} \rightarrow \mathbb{R}^n$. By construction, $\tau_0 \ll t_0$, such that the slow CDE spans a longer integration horizon, while the fast CDE resolves shorter-term dynamics. Both CDEs

integrate over control paths $\mathbf{Y}(\tau)$ and $\hat{\mathbf{X}}(t)$, whose construction will be detailed in Sec. 4.4, where $\mathbf{Y}(\tau)$ is generated via a path transformation and $\hat{\mathbf{X}}(t)$ incorporates the interpolated slow state $\mathbf{d}(\tau(t))$ obtained from Eq. (6).

Solving these CDEs involves two aspects of multiscale: multi-rate sampling of the data and multi-step numerical integration for each timescale. As shown in Fig. 1, the slow CDE Eq. (6) operates on coarsely sampled data to capture gradual degradation dynamics g_ϕ , while the fast CDE Eq. (7) uses finely sampled data to model rapid operational dynamics f_θ . The construction of these data sequences will be detailed in Sec. 4.6. This separation allows the use of multiscale numerical step sizes, larger for long horizon degradation accumulation and smaller for rapid operational fluctuations, which reduces stiffness and improves training efficiency.

Finally, we introduce a readout mapping $\chi_\theta : \mathbb{R}^m \rightarrow \mathbb{R}^n$ that predicts the next system state $\hat{\mathbf{x}}(t+1)$ from the latent fast state $\mathbf{z}(t)$.

4.4. Degradation Path Transformation and Construction

We first define the slow control path $\mathbf{Y}(\tau)$, which drives the degradation dynamics g_ϕ in Eq. (6). Direct interpolation of raw observations $(\mathbf{z}_i, \mathbf{u}_i, \tau_i)$, as commonly done in standard CDEs (Sec. 3.2), is insufficient here since these fast states and inputs do not directly capture latent physical processes, such as stress, fatigue, or wear, that govern degradation rates. Moreover, the observed states evolve on a much faster timescale than degradation.

To address this, we introduce a **Degradation Path Transformation**. A learned mapping h_ψ transforms observed states and control inputs at each slow-time τ_i into degradation-relevant features:

$$\mathbf{y}_i = h_\psi(\mathbf{x}_i, \mathbf{u}_i, \tau_i) \quad \text{for } \tau_i \in [\tau_0, T]. \quad (8)$$

These transformed features \mathbf{y}_i are then interpolated with a smooth interpolation scheme (e.g. natural cubic splines) over the sequence $\{(\mathbf{y}_i, \tau_i) \mid \tau_i \in [\tau_0, T]\}$ to construct a continuous path $\mathbf{Y}(\tau)$. This differentiable trajectory serves as input to the fast CDE, enabling operation dynamics modeling that is both driven by control input and degradation-aware.

Next, we construct the fast control path $\hat{\mathbf{X}}(t)$, which drives the operational dynamics f_θ in Eq. (7). Unlike the slow control path $\mathbf{Y}(\tau)$, which requires a path transformation due to unobserved degradation drivers, the fast dynamics is captured directly from observable system states $\mathbf{x}(t)$, control inputs $\mathbf{u}(t)$, and the interpolated degradation state $\mathbf{d}(\tau(t))$. Accordingly,

$\hat{\mathbf{X}}(t)$ is obtained by interpolating $\{[\mathbf{x}_i, \mathbf{u}_i, \mathbf{d}(\tau(t_i)), t_i] \mid \tau_i \in [t_0, T]\}$. where $\mathbf{d}(\tau(t_i))$ aligns with the slow degradation trajectory at the fast-time index t_i . The resulting continuous path serves as the control path for the fast CDE, capturing fast system behavior conditioned on long-term degradation.

4.5. Monotonicity Constraint for Degradation Dynamics

A fundamental property of degradation is that it accumulates over time and is non-decreasing. To ensure our model respects this property and remains numerically stable during integration, the degradation rate $g_\phi d\mathbf{Y}$ in Eq. (7) should ideally satisfy the following three conditions:

1. **Non-negativity:** ≥ 0 , enforcing the monotonic growth of degradation.
2. **Boundedness:** The rate must remain within a limited range to prevent excessively large growth during long horizon integration.
3. **Zero response:** $g_\phi(\cdot)d\mathbf{Y} = 0$, whenever $d\mathbf{Y} = 0$ (no driving) or $g_\phi(\cdot) = 0$ (no sensitivity), ensuring no change in degradation.

This can be achieved by applying an activation function to $g_\phi d\mathbf{Y}$. Standard activation functions fail to meet all these criteria simultaneously (e.g., ReLU/Softplus are unbounded; Sigmoid does not preserve zero response). We therefore propose a new activation function to address these requirements:

$$\sigma(x) = \text{sigmoid}(\gamma x) \cdot \tanh(x), \quad (9)$$

where $\text{sigmoid}(\cdot)$ is the sigmoid function, $\tanh(\cdot)$ is the hyperbolic tangent, and $\gamma \gg 1$ is a hyperparameter. This function is strictly bounded within $(-1, 1)$ and satisfies $\sigma(0) = 0$, and with large γ , the term $\text{sigmoid}(\gamma x)$ approach zero rapidly for $x < 0$ and so for $\sigma(x)$, effectively suppressing negative outputs. While $\sigma(x)$ is not strictly non-negative, this effect can be controlled through the choice of γ .

4.6. Model Training and Degradation Inference

The data are sampled at two rates. A *long coarse sequence* $\{(\mathbf{x}_i, \mathbf{u}_i, t'_i)\}_{i=0}^N$, with a large sampling interval Δt_s captures slow degradation dynamics over $[T_s, T]$, while a *short dense sequence* $\{(\mathbf{x}_j, \mathbf{u}_j, t_j)\}_{j=0}^M$ with a small sampling interval Δt_f , captures rapid operational dynamics over $[T_f, T]$. Both sequences end at the time T ($t_M = t'_N = T$), but differ in resolution ($\Delta t_s \gg \Delta t_f$), sequence length ($N \gg M$), and starting times ($T_s \ll T_f$). Based on

the observation up to time T , the model predicts the next fast state $\hat{\mathbf{x}}(t_{M+1})$ with $t_{M+1} = t_M + \Delta t_f$.

Model parameters are optimized by minimizing a multi-step rollout loss \mathcal{L} . Given history up to time $T = t_M$, the H-CDE model predicts $\hat{\mathbf{x}}(t_j)$ for $j = 1, \dots, M + 1$, and \mathcal{L} measures the discrepancy with ground truth observations \mathbf{x}_j :

$$\mathcal{L}(\theta, \phi, \psi, \dots) = \frac{1}{M+1} \sum_{j=1}^{M+1} \|\mathbf{x}_j - \hat{\mathbf{x}}(t_j)\|^2. \quad (10)$$

By learning to forecast the observable fast states, the model implicitly captures the latent degradation dynamics g_ϕ and path transformation h_ψ , yielding the inferred degradation trajectory $\hat{\mathbf{d}}(\tau)$.

5. Case Studies

To demonstrate the effectiveness and adaptability of the proposed Hierarchical CDE (H-CDE) framework, we evaluate its performance on two distinct case studies: a simulated bridge undergoing stiffness loss due to dynamic traffic and thermal loading (Sec. 5.1), and the benchmark N-CMAPSS turbofan engine dataset, where performance degrades in flow and efficiency (Sec. 5.2). These systems were specifically chosen as they represent different underlying degradation processes and dynamical characteristics, with the bridge exhibiting dynamic response behavior and the engine operating under steady-state conditions, enabling a comprehensive evaluation of H-CDE across diverse domains.

5.1. Degrading Bridge as a Damped Euler–Bernoulli Beam

In the first case study, we model a simplified wooden bridge as a two-dimensional, simply supported Euler–Bernoulli beam with realistic material and geometric properties (detailed in Appendix [Appendix A.1](#)). Degradation, modeled as a loss of material stiffness, is initiated when the beam’s vertical displacement exceeds a defined threshold. The bridge is subjected to a uniformly distributed vertical load representing railway traffic and a thermal load representing thermal expansion and bending due to ambient temperature variations.

5.1.1. Dynamics Modeling

The bridge dynamics are governed by the following equation of motion

$$\mathbf{M} \ddot{\mathbf{x}}(t) + \mathbf{C} \dot{\mathbf{x}}(t) + \mathbf{K} \mathbf{x}(t) = \mathbf{f}(t), \quad (11)$$

where $\mathbf{x}(t)$ represents the nodal degrees of freedom (axial displacement, vertical displacement, and rotation), and $\mathbf{M}, \mathbf{C}, \mathbf{K}$ are the global mass, damping, and stiffness matrices, respectively. We use the Newmark–beta method with sub-stepping to solve the structural dynamics. Damping follows the Rayleigh model, $\mathbf{C} = \alpha_{\text{damp}} \mathbf{M} + \beta_{\text{damp}} \mathbf{K}$, with coefficients set to achieve moderate damping ($\approx 4 - 5\%$ for the fundamental vibration mode). Specific parameter values are listed in [Appendix A.1](#).

5.1.2. Load Modeling

The load vector $\mathbf{f}(t)$ includes the uniformly distributed vertical load $q(t)$ and the thermal loading $\mathbf{f}_T(t)$. The vertical load $\mathbf{q}(t)$ reflects realistic railway traffic load patterns based on statistical data, while the thermal load $\mathbf{f}_T(t)$ accounts both for thermal expansion from overall temperature changes and thermal bending due to temperature gradients across the beam depth, derived from real meteorological temperature measurements. Details on input load and temperature profile generation, as well as thermal load computation, are provided in [Appendix A.1](#).

5.1.3. Degradation Modeling

Structural degradation is captured by a scalar damage variable $D \in [0, 1]$, where $D = 0$ corresponds to an undamaged state and $D = 1$ indicates complete stiffness loss. At each time step, we compute the absolute vertical displacement v_{\max} at mid-span $v_{\max} = \max_{\text{mid-span}} |v(t)|$. If v_{\max} exceeds a reference threshold U_{ref} , the damage increment is given by $\Delta D = \beta_{\text{damage}} (1 - D) ((v_{\max} - U_{\text{ref}})/U_{\text{ref}})^p$; otherwise, $\Delta D = 0$. The accumulated damage D reduces the effective material stiffness through $E_{\text{eff}} = E (1 - D)$ and $I_{\text{eff}} = I (1 - D)$. The parameters governing damage evolution ($U_{\text{ref}}, \beta_{\text{damage}}, p$) are provided in [Appendix A.1](#).

5.1.4. Dataset Generation and Split

We generated 12 bridge run-to-failure trajectories, each simulated until approximately 30% stiffness reduction. Due to computational constraints, the material properties were chosen such that the simulated bridges would fail

after about 2.5 months of operation, which also ensured larger environmental variations across different units. The simulations cover two operational scenarios, both based on realistic railway traffic patterns and real ambient temperature data from different years, designed to evaluate generalization and out-of-distribution (OOD) performance. Scenario A represents moderate daily load peaks with real meteorological data from one year, yielding five training trajectories and one in-distribution test trajectory. Scenario B introduces sharper daily load peaks with temperature data from a different year, yielding six OOD test trajectories. The increased load variations in Scenario B led to different dynamic responses, making it a challenging test case. Each trajectory simulates approximately two months of operational life. For downstream learning tasks, we extracted time series samples every 10 minutes, including displacements at quarter-, third-, and mid-span locations, the applied external load, and the ambient temperature. The complete data generation process is described in Appendix [Appendix A.1](#).

5.2. *Turbofan Engine Degradation (N-CMAPSS)*

5.2.1. *Dataset Description and Split*

For the second case study, we utilize the NASA New Commercial Modular Aero-Propulsion System Simulation (N-CMAPSS) dataset [42], which simulates turbofan engine degradation under realistic flight conditions. We focus on subset DS01, which involves a single component deterioration mode: High-Pressure Turbine (HPT) efficiency modifier. This enables us to treat the HPT efficiency modifier to serve as the ground-truth degradation state, in contrast to other subsets where multiple degradation mechanisms are present.

To simplify evaluation, we consider only trajectory segments after the fault onset, corresponding to the exponential degradation phase, while excluding the initial linear progression and transition region. Additionally, since accelerated degradation is modeled at the flight level and held constant within each flight (i.e., independent of intra-flight operating conditions), the data represents degradation as discrete per-cycle updates rather than continuous degradation dynamics. Since the operating profile of a cycle differs across flight classes in both duration and load, these updates are not generalizable across classes. To avoid this dataset-induced complication, we restrict our analysis to a single flight class. Specifically, we focus on short-flight trajectories in DS01, providing a controlled setting for evaluating the model’s ability to disentangle slow degradation from fast operational variations.

We adopt a standard unit-based split; engine units 1, 4, and 7 are used for training, while Unit 9, which exhibits the fastest degradation among the four, is reserved for testing.

5.2.2. Dynamics Modeling and Model Adaptation

The N-CMAPSS model can be viewed as a discrete-time dynamical system that reaches equilibrium at each operating point, producing steady-state engine outputs given the current inputs and health state [42]:

$$[\mathbf{x}_s(t), \mathbf{x}_v(t)] = f(\mathbf{u}(t), \theta(t)), \quad (12)$$

where $\mathbf{u}(t)$ denotes control inputs (e.g., altitude, Mach number, throttle angle, and inlet temperature), and $\theta(t)$ contains health-related parameters (e.g., the HPT-efficiency modifier). The model outputs include observable physical properties $\mathbf{x}_s(t)$ and latent internal states $\mathbf{x}_v(t)$, the latter serving as virtual sensors not accessible through direct measurements. Following fault onset, accelerated degradation is modeled by updating $\theta(t)$ between flight cycles via a stochastic exponential decay applied to component flow capacities and efficiencies.

To align with this system dynamics, we adapt the fast dynamics module of the H-CDE (Eq. 7) by removing the dependence of $d\mathbf{x}/dt$ on $\mathbf{x}(t)$, since the N-CMAPSS outputs are generated directly from inputs and the degradation state. We modify the inputs to f_θ in Eq. 7, making $\mathbf{u}(t)$ and $\mathbf{d}(t)$ the primary drivers for $d\mathbf{x}(t)/dt$ via the control path $\mathbf{Z}(t)$.

6. Experimental Setup

This section outlines the experimental design used to assess the quality of inferred latent degradation states by the proposed method. We describe the setup and configuration of the residual-based baseline in Sec. 6.1, define the evaluation metrics for latent degradation quality in Sec. 6.1, and provide details on training setups, data preprocessing configurations, hyperparameters, as well as hardware specifications in Sec. 6.4.

6.1. Baseline: Residual-based Model

We compare H-CDE against a residual-based baseline that infers degradation indirectly by measuring deviations from a model of healthy system behavior. Specifically, we adopt the operating-condition-based residual model

from [14], which is widely used and has demonstrated strong empirical performance. This involves training a Feedforward Neural Network (FNN) exclusively on data from the healthy operational phase to learn the mapping from control inputs \mathbf{u} to operational states \mathbf{x} . Depending on the nature of system dynamics (i.e, steady-state vs dynamic response systems), the model may also incorporate a history of past states \mathbf{x} as additional input. The prediction error (residual) on new data then serves as a degradation indicator.

For the bridge case study, where the system dynamics explicitly depend on the current state and no purely healthy samples are available, we approximate healthy behavior using the first 1000 samples (approximately 10% of each trajectory). We train an FNN to predict the current state $\hat{\mathbf{x}}_k$ from a flattened sequence of the past $w - 1$ states $\{\mathbf{x}_j\}_{j=k-w+1}^{k-1}$ and the sequence of w control inputs $\{\mathbf{u}_j\}_{j=k-w+1}^k$. For the N-CMAPSS case study, where system dynamics are primarily driven by control inputs and healthy cycles are labeled, we train an FNN on healthy data to learn a direct mapping from current control input \mathbf{u}_k to the current state $\hat{\mathbf{x}}_k$.

6.2. Evaluation Metric

To assess the quality of the learned latent degradation state, we introduce an **Alignment Score** that measures its linear correlation with the true degradation. Prior works typically focus on health index construction, where degradation is represented as a scalar value and evaluated using dedicated metrics. These metrics, however, are not directly applicable in our setting, since the extracted degradation states can be high-dimensional. The core idea of the proposed metric is that a well-disentangled representation should allow the true degradation to be recovered through a simple linear transformation. Concretely, we train a linear regression model on the latent representations from the training set to predict the true degradation, and then apply the learned regressor to the test set. The **Alignment Score** is defined as the coefficient of determination (R^2) between the predicted and true degradation values on the test set.

6.3. Ablation Studies

To assess the contribution of individual components in our proposed model, we evaluate the following variants in both case studies:

- **w/o MC**: Removes the monotonic constraint on the learned degradation states, allowing non-monotonic degradation trajectories.

- **w/o PT**: Removes the path transformation applied to the input data prior to the CDE integration.

6.4. Implementation Details

6.4.1. Data Processing Configuration

The bridge dataset is sampled at 1 Hz, while the N-CMAPSS dataset was downsampled to 0.1 Hz following the recommendation of Arias Chao et al. [42]. For the residual model, we performed a sweep over input window sizes $w \in \{3, 5, 10, 20\}$. The best performance on the bridge dataset was achieved with $w = 5$. For N-CMAPSS, we set $w = 5$, consistent with its steady-state system dynamics and prior work [14]. Additionally, we tuned the healthy data hold-out length, exploring values of 500, 1000, and 2000, and selected 1000 as optimal.

For H-CDE, inputs are constructed as multiscale sequences. In the bridge case study, we use a slow sequence of length $w_s = 100$ with time step $\Delta t_s = 12$ and a fast sequence of length $w_f = 11$ with $\Delta t_f = 1$, both generated with a sliding window stride of two. The slow sequence length $w_s = 100$ was fixed, and $\Delta t_s = 12$ was chosen to span approximately 10% of the full run-to-failure trajectory. The fast sequence length $w_f = 11$ was selected to align with the final slow step time interval. The stride was set to two to reduce the volume of training data. In the N-CMAPSS case study, the slow sequence also uses $w_s = 100$, but with $\Delta t_s = 20$, and the fast sequence uses $w_f = 5$ with $\Delta t_f = 2$, generated with a stride of five. The slow sequence configuration was chosen to roughly span three short flight cycles. For fast sequence length w_f , we compared lengths of five and ten, and selected $w_f = 5$ based on better empirical performance.

6.4.2. Model Hyperparameter Tuning

Residual (Bridge: 4,963 params; N-CMAPSS: 4,184 params). We employ a Feedforward Neural Network (FNN) with 4 hidden layers, using SiLU activation, batch normalization, and a dropout rate of 0.2. The hidden layer dimensions were selected from the same search space $\{[20, 20, 20, 10], [100, 100, 50, 20], [50, 50, 20, 10]\}$, with $[50, 50, 20, 10]$ yielding the best performance across both datasets.

H-CDE (Bridge: 23,268 params; N-CMAPSS: 16,636 params). To reduce the hyperparameter search space, we applied the same configuration to both slow and fast CDE layers. Each CDE layer uses 2-layer MLPs for the vector fields and readout heads. We explored hidden dimensions of 64 and

128 and found 64 to yield better performance for both case studies. Similarly, we fine-tuned the latent dimensions between 10 and 20, with 10 yielding the best results in both cases. For the N-CMAPSS dataset, the latent dimension of slow CDE was further tuned between five and ten, with five selected as optimal. SiLU activation was used, without batch normalization or dropout. Following common practice for NODE-based models, no explicit initialization was applied due to sensitivity to initial conditions. Both case studies used an explicit adaptive solver dopri5 with relative tolerance $1e^{-3}$ and absolute tolerance $1e^{-5}$.

6.4.3. Training Setups

All models were trained using the AdamW optimizer [43] with an initial learning rate of 5×10^{-3} and a batch size of 256. The models minimize the L2 (Mean Squared Error) loss. From the generated training samples, 20% are randomly held out as a validation set. This validation set is used for early stopping decisions and for learning rate scheduling via ReduceLROnPlateau, which reduces the learning rate by a factor of 0.95 if the validation loss does not improve for five consecutive epochs. For the bridge dataset, training proceeds for a maximum of 30 epochs with early stopping and a minimum of five epochs. For the N-CMAPSS dataset, training runs for a maximum of 60 epochs and a minimum of 20 epochs.

6.4.4. Hardware and Software

All methods were implemented using PyTorch 1.12.1 [44] with CUDA 12.0. Computations for both case studies were executed on a GPU cluster equipped with NVIDIA A100 80GB GPUs. We employed neptune.ai for experiment tracking and management.

7. Results and Discussions

This section presents our experimental results on self-supervised degradation inference. We evaluate the quality of the learned latent representation on two case studies: the **Bridge** dataset, which represents a system with dynamic response (Sec. 7.1), and the **N-CMAPSS** dataset, which represents a steady-state system (Sec. 7.2). Relevant ablation studies analyzing the contribution of individual model components are discussed within each subsection.

7.1. Bridge Case Study

We first examine the embedding space of the residuals from the residual method and the latent degradation states from H-CDE and its variants on the bridge dataset, as shown in Fig. 2. For the residual method, all residuals are reduced to two dimensions using PCA for visualization purposes, and the latent states from H-CDE and its variants are projected in the same way. The plots show the first two principal components (PCs), for representative training (unit 1), in-distribution (ID) test (unit 3), and out-of-distribution (OOD) test units (unit 9). The first two units share the same load distribution, whereas the last differs. The specific train–test split was described in Sec. 5.1.4. To quantify the quality of these embedding spaces, we report the alignment score as defined in Sec. 6.2 in Tab. 1. A detailed comparison of the extracted latent degradation representations is presented in Sec. 7.1.1, followed by the ablation study results in Sec. 7.1.2, which analyze the impact of the monotonicity constraint, path transformation, and slow time step size on both alignment score and the computational cost.

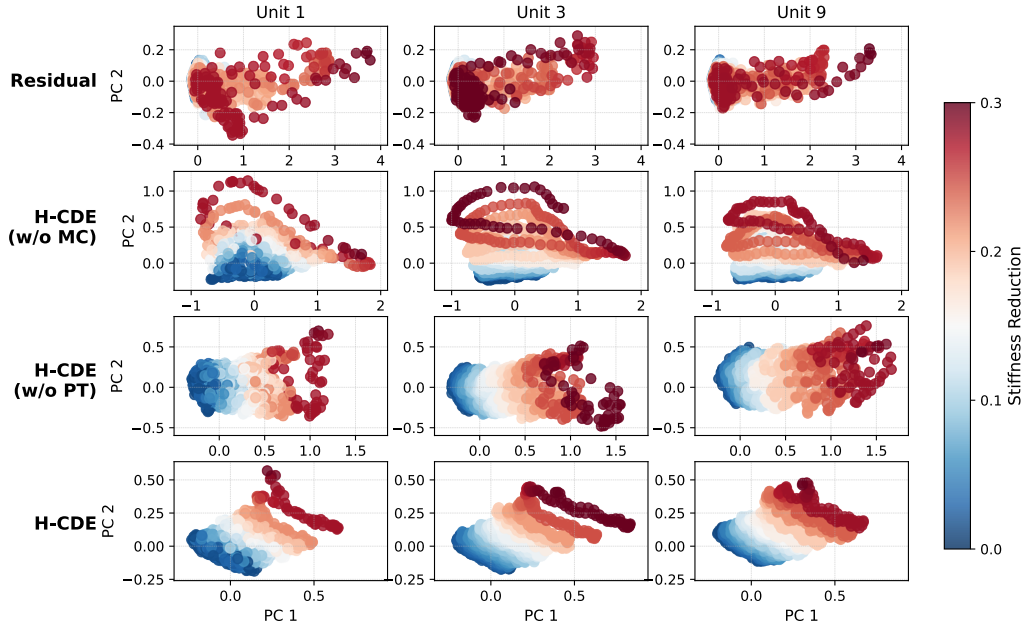


Figure 2: First two principal components (PCs) of embedding space for selected units in the bridge dataset (Training Unit 1, ID Test Unit 3, OOD Test Unit 9). Colors indicate true degradation (stiffness reduction).

Table 1: Alignment Score (R^2) on in-/out-of-distribution runs.

Method	In-Distribution	Out-of-Distribution
Residual	0.324 ± 0.054	0.282 ± 0.036
H-CDE (w/o MC)	0.969 ± 0.010	0.941 ± 0.033
H-CDE (w/o PT)	0.954 ± 0.010	0.820 ± 0.045
H-CDE	0.967 ± 0.007	0.941 ± 0.018

7.1.1. Comparison of Latent Degradation Representation

Limitations of the residual-based method. As shown in Fig. 2, the embedding space derived from the residuals provides limited information about the true degradation. This is consistent with the low alignment score reported in Tab. 1. Although the FNN with past state inputs can model healthy system dynamics reasonably well, the residuals do not directly represent the degradation state. In the literature, residuals, or their distributions, are often used as a proxy for degradation level [45]. However, this approach does not account for the dynamic responses, and the residuals therefore fail to capture the nonlinear effects of degradation on sensor measurements, leaving these effects entangled with the load and temperature history.

H-CDE: Meaningful degradation embedding and generalization. Compared with the residual baseline, the H-CDE embeddings in Fig. 2 form a rectangular manifold on which the degradation trend is clearly visible, indicating successful disentanglement and physically meaningful latent states. The enlarged spacing toward the end of the trajectory suggests an accelerating degradation rate as the system approaches the end of operational life, consistent with the expected accelerated stiffness loss in the underlying physical model. The embeddings are consistent across training, in-distribution test, and OOD test units, which aligns with the results in Tab. 1, where H-CDE achieves the highest alignment score for both cases. This consistency demonstrates strong generalization to varying and unseen operating and environmental conditions. A notable observation is that, although PC1 explains most of the variance, the degradation trajectory is inclined in the (PC1, PC2) plane. We hypothesize that this tilt arises from modeling the underlying second-order damped dynamics (Eq.(11)) with a first-order CDE for the fast dynamics (Eq.(7)). Unmodeled second-order dynamics may introduce additional first-order operational variations into the latent states, leading to this oblique manifold. While accurately modeling the fast system

dynamics is beyond the scope of this work, which focuses on disentanglement, future research could explore higher-order NODEs [46] into the fast CDE to better capture these dynamics and potentially improve performance.

7.1.2. Ablation Studies and Sensitivity Analysis

Table 2: Ablation study of H-CDE: slow CDE number of function evaluations (NFE).

Method	In-Distribution	Out-of-Distribution
H-CDE	689 ± 5	631 ± 93
H-CDE (w/o MC)	712 ± 11	996 ± 109
H-CDE (w/o PT)	686 ± 1	748 ± 44

Impact of monotonicity constraint. Although the alignment score of the w/o MC variant is close to that of H-CDE (Tab. 1), its embedding space in Fig. 2 differs substantially. Without the monotonicity constraint, the magnitude of the latent states no longer predominantly increases with the degradation state. Furthermore, PC1 no longer aligns with the primary degradation trend, which instead appears along PC2, indicating that the embedding space is still dominated by operational variations. Moreover, the embeddings for training and test units differ more noticeably, indicating reduced generalization. This is also reflected in Tab. 2, where w/o MC requires significantly more function evaluations (NFE), particularly for OOD data (about 58% higher), thereby increasing computational cost. Overall, the monotonicity constraint yields more interpretable degradation representations and acts as a valuable regularizer, guiding optimization toward stable solutions with lower NFE and physically consistent degradation dynamics.

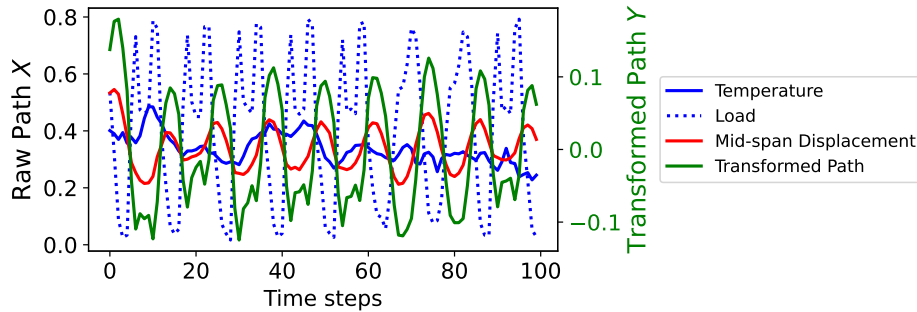


Figure 3: Path transformation for a sample from the bridge dataset.

Impact of path transformation. Removing the path transformation (w/o PT) has a greater impact on the alignment score than removing the monotonicity constraint, particularly for the OOD subset (Tab. 1). In Fig. 2, the overall embedding structure of w/o PT is similar to that of H-CDE, with PC1 capturing most of the degradation variance. However, the shape suggests some unexplained variance from a third dimension, and the OOD embeddings differ more noticeably, which is consistent with the lower score in Tab. 1. In terms of computational cost, the w/o PT variant requires more NFEs than H-CDE for both ID and OOD cases. The path transformation maps raw operational states to latent factors driving slow degradation, thereby isolating degradation drivers from irrelevant operational variations. Without it, solving the slow CDE becomes more difficult and the model generalizes less effectively. To illustrate this isolation effect, Fig. 3 shows the raw input path for a sample (temperature, load, and displacement) alongside the learned transformed path. The transformation originally produces 10 latent dimensions; here, only the primary component after PCA is shown. Notably, this primary transformed path does not track variations in load or temperature but more closely resembles the displacement signal, with narrower peak regions. This behavior is consistent with the physical degradation process, where degradation accumulates when displacement exceeds a threshold, indicating that the PT module effectively extracts displacement-related information as the key degradation driver. By isolating the most relevant driver, the path transformation likely contributes to improved generalization of H-CDE across operating and environmental conditions.

Impact of slow time step size. In this sensitivity analysis, we vary the slow time step size Δt_s while keeping the fast time step size ($\Delta t_f = 1$) and the fast window size ($w_f = 100$) fixed, thereby changing the total time interval covered without altering the number of input samples. We evaluate $\Delta t_s \in \{1, 3, 6, 12\}$, stopping at 12 as it corresponds to roughly 10% of the service life; larger values would require more data and reduce usability. The resulting alignment score and NFE are shown in Fig. 4. The alignment score generally increases with Δt_s for both ID and OOD subsets, indicating that longer temporal contexts help capture degradation progression. For ID subset, high alignment scores are already achieved at $\Delta t_s = 3$, while the OOD subset requires larger steps ($\Delta t_s \approx 6$) to reach comparable scores, suggesting that longer-range dependencies are more critical for generalization. In terms of computational cost (NFE), ID subset remains stable across Δt_s , whereas OOD cost decreases when $\Delta t_s \geq 3$. One possible explanation is that

the coarser, “rougher” path representation from larger steps is sufficient to capture the degradation progression while simplifying the dynamics for the adaptive ODE solver, reducing noise and complexity [36], thereby improving generalization. Overall, Δt_s controls a trade-off between data requirements and the ability to better extract latent degradation trends.

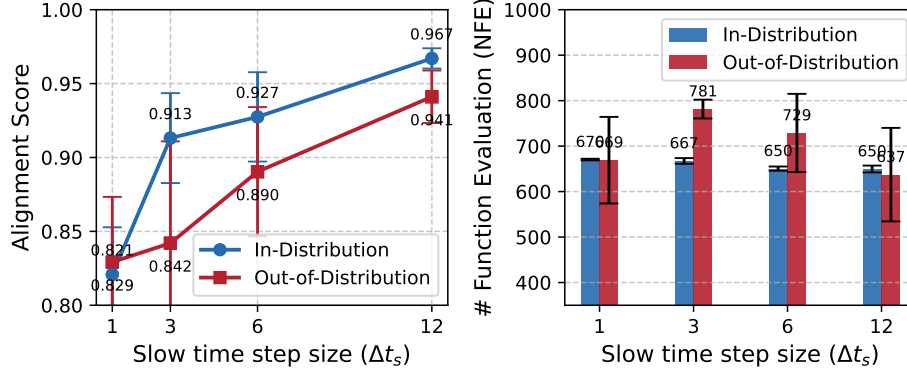


Figure 4: Sensitivity of H-CDE performance to the slow time step size (Δt_s) in the bridge case study.

7.2. N-CMAPSS Case Study

For the N-CMAPSS case study, we qualitatively and quantitatively analyze the embedding space of both residual-based methods and H-CDE, along with its variance, following the same procedure as in the bridge case (see Fig. 5, Tab. 3). To assess the practical utility of the degradation embeddings, we evaluate the alignment score of the first principal component (PC1), from which a potential health index can be derived when full run-to-failure trajectories are available. Predicted degradation state (efficiency modifier) derived from either all latent dimensions or PC1 alone is shown in Fig. 6, with corresponding alignment scores reported in Tab. 3. These results are discussed in Sec. 7.2.1, with additional ablation studies in Sec. 7.2.2.

7.2.1. Comparison of Latent Degradation Representation

Residual baseline: entanglement with operating conditions. The embedding extracted by the residual method in Fig. 5 better reveals the degradation trend than in the bridge case, with PC1 roughly reflecting the degradation level in Fig. 6. However, it remains noisy, with fluctuations

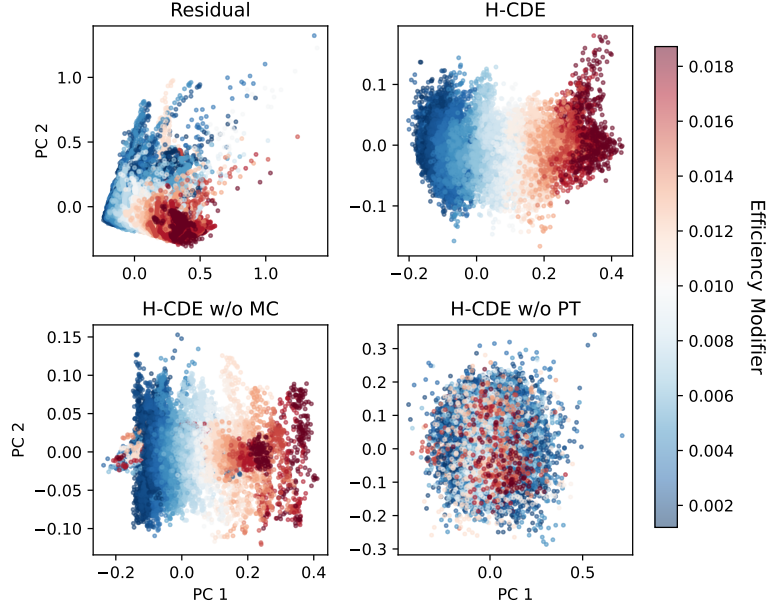


Figure 5: Latent degradation states of the test unit 9 from the N-CMAPSS dataset, projected onto PC1/PC2, shown across five random seeds.

appearing to reflect operational cycles. When using only PC1, these fluctuations become more pronounced, as also seen in the lower alignment score in Tab. 3. This indicates that the residual-based method cannot effectively disentangle degradation from operational variations. This limitation arises from its assumption that sensor measurements under degradation can be expressed as a linear combination of healthy behavior and degradation effects, i.e., $\mathbf{r}_k = \mathbf{x}_k - \hat{\mathbf{x}}_k \approx g(\mathbf{u}_k, \mathbf{d}_k) - f(\mathbf{u}_k)$, which implies $\mathbf{x}_k = f(\mathbf{u}_k) + \mathbf{d}_k$. In reality, degradation and control inputs interact nonlinearly in the true system dynamics $g(\mathbf{u}_k, \mathbf{d}_k)$ [15]. These unmodeled nonlinear dependencies remain entangled with operating history, leading to noisy estimates. Compared to the bridge case, the residual method performs better on N-CMAPSS since it is a steady-state system where $\mathbf{x}(t)$ depends directly on $\mathbf{u}(t)$ and $\mathbf{d}(t)$, without derivative terms. This reduces entanglement and yields clearer embeddings.

H-CDE: accurate degradation representation. In comparison, the H-CDE embedding is much more structured, with PC1 capturing most of the degradation variance in Fig. 5. This is also evident in Fig. 6, where the predicted degradation closely matches the ground truth, even when using only PC1. Unlike the residual baseline, the predictions are stable within opera-

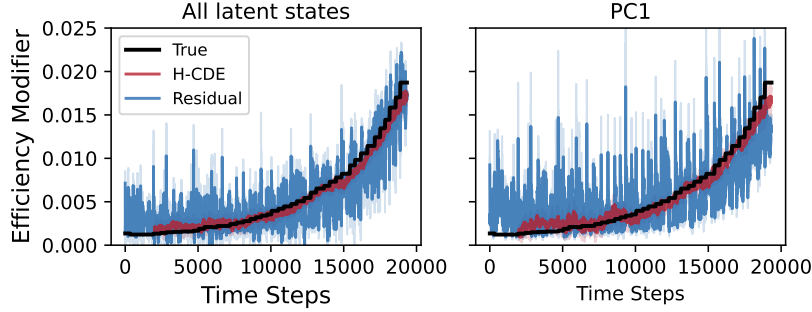


Figure 6: Predicted degradation (efficiency modifier) for N-CMAPSS using linear regression on H-CDE latent states versus baseline residuals. Left: predictions from all latent dimensions. Right: predictions using only the first principal component (PC1)

tional cycles. This is consistent with the quantitative results in Tab. 3, where H-CDE achieves about 20% higher alignment score than the baseline when using all latent states/residuals, and an even larger improvement of around 64% when using only PC1. These high alignment scores validate that the learned degradation representation generalizes well to the new test unit with different operating cycles. Finally, the comparable alignment scores from all states and from PC1 show that a simple dimensionality reduction method such as PCA can yield a scalar degradation representation, from which a health index can be derived when run-to-failure trajectories are available, highlighting the practical utility of H-CDE.

7.2.2. Ablation Studies

We now examine the ablation studies on the N-CMAPSS dataset. Compared to the bridge case, the impact of PT and MC is much larger. To better understand this behavior, we additionally visualize the learned degradation trajectories $\mathbf{d}(\tau)$ in Fig. 7. Each trajectory corresponds to one data sample, colored by its final degradation level, with a sequence length matching the slow-sequence window size. The endpoint of each trajectory in Fig. 7 corresponds to a point in the embedding space shown in Fig. 5. The following summarizes the main insights from these ablation results.

Degradation trajectories of H-CDE. For H-CDE, the trajectories exhibit clear separation according to the degradation level and progress monotonically along the primary degradation axis (PC1) over time. The rate of this progression varies based on the trajectory’s degradation level: trajectories with higher degradation progress more rapidly, diverging from healthier

ones and converging to distinct, separable endpoints in Fig. 7. Interestingly, the learned trajectories resemble exponential curves, consistent with the underlying physical degradation process.

Impact of path transformation. Path transformation proves to be critical in this case study. The w/o PT variant achieves near-zero alignment scores in Tab. 3 and yields an uninterpretable embedding space in Fig. 5. The latent trajectories in Fig. 7 explain this failure: along the primary degradation axis (PC1), they first briefly decrease before increasing, breaking monotonic progression. This occurs despite the MC constraint, due to the small negative range permitted by the activation function (see Eq.9). As a result, trajectory endpoints collapse into a single region, indicating that the model fails to capture physically meaningful degradation paths and to separate degradation levels. These findings highlight path transformation as a key mechanism for isolating degradation drivers from dominant operational dynamics and enabling the model to learn the degradation process. Its impact is notably stronger in N-CMAPSS than in the bridge case. This increased sensitivity can be attributed to two factors: (i) in the bridge dataset, the main degradation-related state (displacement) is directly measured, reducing the need for PT; and (ii) N-CMAPSS has a higher-dimensional sensor space with hidden degradation drivers, making PT essential for isolating key degradation drivers.

Table 3: Alignment Score for Different Ablation Settings

Model	All latent states	PC1
Residual	0.802 ± 0.024	0.566 ± 0.072
CDE (w/o MC)	0.820 ± 0.219	0.691 ± 0.374
CDE (w/o PT)	0.003 ± 0.064	-0.026 ± 0.057
CDE	0.964 ± 0.010	0.928 ± 0.028

Impact of the monotonicity constraint. Removing the monotonicity constraint has a smaller impact than removing path transformation, but it still noticeably degrades the performance compared to the full H-CDE model. The effect is most evident when using only PC1, where alignment scores are lower and exhibit higher variance as reported in Tab. 3. This instability reflects inconsistent separability in the learned latent space across runs, as shown in Fig. 5. This behavior can be explained by inspecting the latent trajectories in Fig. 7: in failed runs, the w/o MC variant exhibits

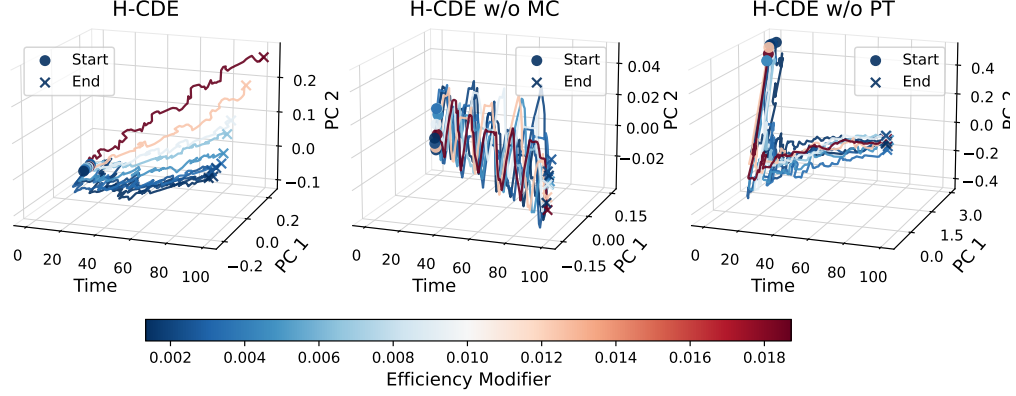


Figure 7: Degradation trajectories $\mathbf{d}(\tau)$ in the N-CMAPSS ablation study. Each trajectory represents one sample, colored by its final degradation level (efficiency modifier).

cyclic patterns that resemble operational cycles, indicating a stronger influence from operational variations than degradation progression. Without the monotonicity constraint, the model struggles to enforce a clear degradation trend, leading trajectories to collapse toward a common region and reducing state separability. This challenge is amplified in the N-CMAPSS case study because degradation remains constant within each operational cycle (a simulation limitation) and only changes between cycles. The strong cycle-to-cycle operational variation makes it difficult for the model to infer the slow underlying progression without explicit guidance. The monotonicity constraint therefore plays a crucial role in stabilizing training, improving embedding quality, and ensuring a physically consistent degradation trajectory.

8. Conclusion

This paper proposes the Hierarchical Controlled Differential Equation (H-CDE) framework, a novel approach for disentangling degradation from operational dynamics in sensor data. H-CDE models degradation and operational states as coupled slow-fast dynamics, parameterized by separate Controlled Differential Equations (CDEs). Its key contributions include an efficient multi-scale integration scheme to mitigate numerical stiffness, a learnable path transformation to derive latent degradation drivers as the control path in the slow degradation CDE, and a monotonicity constraint in the degradation progression, implemented through a custom activation func-

tion that regularizes disentanglement. We investigated two representative systems: bridges, which exhibit dynamic responses, and aero-engines, which operate in steady states, where most existing research has focused. Experiments demonstrated H-CDE’s ability to capture long-range dependencies and multi-scale dynamics, consistently outperforming residual-based baselines on both system types. Qualitative analysis of the learned degradation embeddings and quantitative alignment with true degradation states confirmed its effectiveness, while ablation studies highlighted the importance of the path transformation and monotonicity constraint. We further highlighted the limitations of widely used residual-based methods, which model the system state under degradation as a linear superposition of the state under healthy conditions and a degradation component. This assumption leads to noisy inference in steady-state systems and fails entirely in dynamic-response systems, where residuals are heavily entangled with operational states.

Overall, this work highlights the need to account for the specific nature of system dynamics in degradation inference. While most methods focus solely on degradation-aware operational dynamics, we show that jointly modeling operational and degradation dynamics enables the introduction of meaningful constraints on degradation, serving as an effective regularizer, enabling more generalizable and physically plausible degradation inference. Nevertheless, the current work focuses on degradation inference under a single failure mode, either as global stiffness loss in a bridge system or as a fault on a single component in an aero-engine system. A natural extension is to systems with multiple failure mechanisms, where different degradation processes may interact and influence each other’s progression. Future work could also explore several other promising directions: investigating log-CDE methods that utilize log-signatures as statistics to potentially improve memory over long horizons, extending the framework to handle higher-order differential equations, exploring the integration of graph neural networks to model spatial dependencies described by PDEs, incorporating explicit physics knowledge within the H-CDE framework, or enhancing the uncertainty quantification of the inferred degradation states.

9. Data and Code Availability

The script we used to generate this synthetic bridge dataset is available in the associated code repository to ensure reproducibility and facilitate further

studies. Our code and data will be available upon acceptance under <https://github.com/EPFL-IMOS/hcde>.

Acknowledgments

This work was supported by the Swiss National Science Foundation under Grant 200021_200461. During the preparation of this work, the authors used ChatGPT to assist with refining and correcting the text. After using this tool, the authors carefully reviewed and edited the content as needed and take full responsibility for the content of this publication.

Appendix A. Details of Case Studies Setups

Appendix A.1. Bridge Simulation Parameters and Details

This appendix provides the specific parameters and further details for the simulated degrading bridge case study discussed in Section 5.1.

Geometry and Discretizations. The bridge model has a total length $L = 10$ m and is discretized into $N_e = 20$ finite elements (21 nodes). Boundary conditions are simply supported (pinned at node 0, roller at node 20).

Material Properties. The initial material properties, representing Medium-Density Fiberboard (MDF), are: Young’s modulus $E = 4.0 \times 10^9$ Pa; moment of inertia $I = 0.0005$ m⁴; cross-sectional area $A = 0.06$ m²; density $\rho = 550$ kg/m³; and thermal expansion coefficient $\alpha = 5 \times 10^{-6}$ K⁻¹.

Damping Parameters. Rayleigh damping ($C = \alpha_{\text{damp}} M + \beta_{\text{damp}} K$) uses coefficients $\alpha_{\text{damp}} = 0.1$ s⁻¹ (mass-proportional) and $\beta_{\text{damp}} = 0.015$ s (stiffness-proportional).

Input Data Generation. *Temperature:* Hourly data (0.1°C precision) from Zurich Fluntern weather station (via Visual Crossing) for 2023 and 2024. *Load:* Based on SBB passenger traffic statistics (Zurich main station, 2024 hourly percentages for short/long distance trains). Daily load factors are derived reflecting these patterns (with random daily variations, standard deviation 0.1). The distributed load $q(t)$ is obtained by applying these factors to a base scaling constant of 36 (resulting units nominally N/m).

Damage Model Parameters. The damage accumulation follows $\Delta D = \beta_{\text{damage}} (1 - D)((v_{\text{max}} - U_{\text{ref}})/U_{\text{ref}})^p$ for $v_{\text{max}} > U_{\text{ref}}$. The parameters are: damage initiation threshold $U_{\text{ref}} = 0.0125$ m (L/800, max absolute vertical displacement); damage scaling parameter $\beta_{\text{damage}} = 3.2 \times 10^{-4}$ (applied per time step Δt); and damage exponent $p = 2$.

Thermal Load Calculation Details. Thermal loads contributing to $F(t)$ include axial forces from uniform temperature change $\Delta T = T_{\text{ambient}} - T_{\text{ref}}$ (with $T_{\text{ref}} = 20^\circ\text{C}$), and bending moments from an effective temperature gradient across the beam depth. This gradient is calculated via an exponential smoothing filter (update factor 0.1) applied to the recent ambient temperature history to represent thermal inertia, and is scaled by $\beta_{\text{thermal}} = 1.0$.

Numerical Integration Scheme. The Newmark–beta integration method (average acceleration scheme with $\beta = 0.25$, $\gamma = 0.5$) is employed. Integration uses a substep time interval $dt_{\text{sub}} = 1$ min within each main input record interval $\Delta t = 10$ min.

Run-to-Failure Simulation Setup. Individual bridge instances start at different starting points, offset by 2 months to capture varying seasonal conditions. Each simulation proceeds until the bridge reaches end-of-life, defined as 30% stiffness reduction ($D \approx 0.3$). Two primary input scenarios are modeled: Scenario A uses 2023 meteorological temperature data combined with a load pattern derived from long-distance traffic statistics, while Scenario B uses 2024 meteorological temperature data combined with a load pattern derived from short-distance traffic statistics (resulting in sharper daily peaks).

References

- [1] B. Zapparoli Cunha, C. Droz, A.-M. Zine, S. Foulard, M. Ichchou, [A review of machine learning methods applied to structural dynamics and vibroacoustic](#), Mechanical Systems and Signal Processing 200 (2023) 110535. doi:10.1016/j.ymssp.2023.110535.
URL <https://www.sciencedirect.com/science/article/pii/S0888327023004430>
- [2] D. Y. Pimenov, A. Bustillo, S. Wojciechowski, V. S. Sharma, M. K. Gupta, M. Kuntoğlu, [Artificial intelligence systems for tool condition monitoring in machining: analysis and critical review](#), Journal of Intelligent Manufacturing 34 (5) (2023) 2079–2121. doi:10.1007/s10845-022-01923-2.
URL <https://doi.org/10.1007/s10845-022-01923-2>
- [3] S. Schwartz, J. J. Montero Jiménez, R. Vingerhoeds, M. Salaün, [An unsupervised approach for health index building and for similarity-based remaining useful life estimation](#), Computers in Industry 141 (2022)

103716. doi:10.1016/j.compind.2022.103716.
 URL <https://www.sciencedirect.com/science/article/pii/S0166361522001130>
- [4] A. Ahmed Murtaza, A. Saher, M. Hamza Zafar, S. Kumayl Raza Moosavi, M. Faisal Aftab, F. Sanfilippo, [Paradigm shift for predictive maintenance and condition monitoring from Industry 4.0 to Industry 5.0: A systematic review, challenges and case study](#), Results in Engineering 24 (2024) 102935. doi:10.1016/j.rineng.2024.102935.
 URL <https://www.sciencedirect.com/science/article/pii/S2590123024011903>
- [5] O. Fink, Q. Wang, M. Svensén, P. Dersin, W. J. Lee, M. Ducoffe, Potential, challenges and future directions for deep learning in prognostics and health management applications, Engineering Applications of Artificial Intelligence 92 (2020) 103678, arXiv: 2005.02144 Publisher: Pergamon. doi:10.1016/J.ENGAPPAI.2020.103678.
- [6] M. Zagorowska, O. Wu, J. R. Ottewill, M. Reble, N. F. Thornhill, [A survey of models of degradation for control applications](#), Annual Reviews in Control 50 (2020) 150–173. doi:10.1016/j.arcontrol.2020.08.002.
 URL <https://linkinghub.elsevier.com/retrieve/pii/S1367578820300559>
- [7] A. Jarosz, M. Zagorowska, J. Baranowski, [Recent advances in data-driven methods for degradation modelling across applications](#), arXiv:2504.18164 [eess] version: 1 (Apr. 2025). doi:10.48550/arXiv.2504.18164.
 URL <http://arxiv.org/abs/2504.18164>
- [8] A. F. Shahraki, O. P. Yadav, a. H. Liao, [A Review on Degradation Modelling and Its Engineering Applications](#), International Journal of Performability Engineering 13 (3) (2017) 299. doi:10.23940/ijpe.17.03.p6.299314.
 URL <https://www.ijpe-online.com/EN/10.23940/ijpe.17.03.p6.299314>
- [9] S. Zhang, Q. Zhai, Y. Li, [Degradation modeling and RUL prediction with Wiener process considering measurable and unobservable external impacts](#), Reliability Engineering & System Safety 231 (2023) 109021.

- doi:10.1016/j.ress.2022.109021.
 URL <https://www.sciencedirect.com/science/article/pii/S0951832022006366>
- [10] Y. Tian, M. A. Chao, C. Kulkarni, K. Goebel, O. Fink, [Real-time model calibration with deep reinforcement learning](#), *Mechanical Systems and Signal Processing* 165 (2022) 108284, publisher: Elsevier BV. doi:10.1016/j.ymssp.2021.108284.
 URL <https://linkinghub.elsevier.com/retrieve/pii/S0888327021006506>
- [11] X. Liu, E. Lunde, F. Diehl, A. Zhang, J. Vatn, S. Yin, [Degradation modeling under time-varying operating conditions: Inference and prognosis with particle filter](#), *Reliability Engineering & System Safety* 245 (2024) 109965. doi:10.1016/j.ress.2024.109965.
 URL <https://linkinghub.elsevier.com/retrieve/pii/S0951832024000401>
- [12] F. Balali, H. Seifoddini, A. Nasiri, [Data-driven predictive model of reliability estimation using degradation models: a review](#), *Life Cycle Reliability and Safety Engineering* 9 (1) (2020) 113–125. doi:10.1007/s41872-020-00111-6.
 URL <https://doi.org/10.1007/s41872-020-00111-6>
- [13] J. Zhou, J. Yang, Y. Qin, [A systematic overview of health indicator construction methods for rotating machinery](#), *Engineering Applications of Artificial Intelligence* 138 (2024) 109356. doi:10.1016/j.engappai.2024.109356.
 URL <https://linkinghub.elsevier.com/retrieve/pii/S0952197624015148>
- [14] C.-C. Hsu, G. Frusque, O. Fink, [A Comparison of Residual-based Methods on Fault Detection](#), in: *Annual Conference of the PHM Society*, Vol. 15, 2023, arXiv:2309.02274 [eess]. doi:10.36001/phmconf.2023.v15i1.3444.
 URL <http://arxiv.org/abs/2309.02274>
- [15] X.-S. Si, T. Li, J. Zhang, Y. Lei, [Nonlinear degradation modeling and prognostics: A Box-Cox transformation perspective](#), *Reliability Engineering & System Safety* 217 (2022) 108120.

- doi:[10.1016/j.ress.2021.108120](https://doi.org/10.1016/j.ress.2021.108120).
 URL <https://www.sciencedirect.com/science/article/pii/S0951832021006165>
- [16] K. Bajarunas, M. L. Baptista, K. Goebel, M. A. Chao, [Health index estimation through integration of general knowledge with unsupervised learning](#), Reliability Engineering & System Safety 251 (2024) 110352. doi:[10.1016/j.ress.2024.110352](https://doi.org/10.1016/j.ress.2024.110352).
 URL <https://www.sciencedirect.com/science/article/pii/S0951832024004241>
- [17] S. Garmaev, O. Fink, [Deep Koopman Operator-based degradation modelling](#), Reliability Engineering & System Safety 251 (2024) 110351. doi:[10.1016/j.ress.2024.110351](https://doi.org/10.1016/j.ress.2024.110351).
 URL <https://www.sciencedirect.com/science/article/pii/S095183202400423X>
- [18] S. Navidi, A. Thelen, T. Li, C. Hu, [Physics-informed machine learning for battery degradation diagnostics: A comparison of state-of-the-art methods](#), Energy Storage Materials 68 (2024) 103343. doi:[10.1016/j.ensm.2024.103343](https://doi.org/10.1016/j.ensm.2024.103343).
 URL <https://www.sciencedirect.com/science/article/pii/S2405829724001703>
- [19] S. Fu, N. P. Avdelidis, [Prognostic and Health Management of Critical Aircraft Systems and Components: An Overview](#), Sensors 23 (19) (2023) 8124, number: 19 Publisher: Multidisciplinary Digital Publishing Institute. doi:[10.3390/s23198124](https://doi.org/10.3390/s23198124).
 URL <https://www.mdpi.com/1424-8220/23/19/8124>
- [20] H. Su, J. Lee, [An Advanced Diagnostic Model for Gearbox Degradation Prediction Under Various Operating Conditions and Degradation Levels](#), Vol. 16, 2024, journal Abbreviation: Annual Conference of the PHM Society Publication Title: Annual Conference of the PHM Society. doi:[10.36001/phmconf.2024.v16i1.3869](https://doi.org/10.36001/phmconf.2024.v16i1.3869).
- [21] M. Arias Chao, [Combining deep learning and physics-based performance models for diagnostics and prognostics](#), PhD Thesis, ETH Zurich (2021). URL <https://www.research-collection.ethz.ch/handle/20.500.11850/517153>

- [22] F. Locatello, S. Bauer, M. Lucic, G. Raetsch, S. Gelly, B. Schölkopf, O. Bachem, [Challenging Common Assumptions in the Unsupervised Learning of Disentangled Representations](#), in: Proceedings of the 36th International Conference on Machine Learning, PMLR, 2019, pp. 4114–4124, iSSN: 2640-3498.
URL <https://proceedings.mlr.press/v97/locatello19a.html>
- [23] P. Kidger, [On Neural Differential Equations](#), arXiv:2202.02435 [cs] (Feb. 2022). doi:10.48550/arXiv.2202.02435.
URL <http://arxiv.org/abs/2202.02435>
- [24] P. Kidger, J. Morrill, J. Foster, T. Lyons, [Neural Controlled Differential Equations for Irregular Time Series](#), arXiv:2005.08926 [cs] (Nov. 2020). doi:10.48550/arXiv.2005.08926.
URL <http://arxiv.org/abs/2005.08926>
- [25] H. Meijer, F. Dercole, B. Oldeman, [Numerical Bifurcation Analysis](#), in: R. A. Meyers (Ed.), Mathematics of Complexity and Dynamical Systems, Springer, New York, NY, 2011, pp. 1172–1194. doi:10.1007/978-1-4614-1806-1_71.
URL https://doi.org/10.1007/978-1-4614-1806-1_71
- [26] Y. Shi, C. R. Rojas, [Efficient Simulation of Singularly Perturbed Systems Using a Stabilized Multirate Explicit Scheme](#), arXiv:2504.06371 [math] (Apr. 2025). doi:10.48550/arXiv.2504.06371.
URL <http://arxiv.org/abs/2504.06371>
- [27] K. T. P. Nguyen, [Feature Engineering and Health Indicator Construction for Fault Detection and Diagnostic](#), in: K. P. Tran (Ed.), Control Charts and Machine Learning for Anomaly Detection in Manufacturing, Springer International Publishing, Cham, 2022, pp. 243–269. doi:10.1007/978-3-030-83819-5_10.
URL https://doi.org/10.1007/978-3-030-83819-5_10
- [28] H. Zhou, X. Huang, G. Wen, Z. Lei, S. Dong, P. Zhang, X. Chen, [Construction of health indicators for condition monitoring of rotating machinery: A review of the research](#), Expert Systems with Applications 203 (2022) 117297. doi:10.1016/j.eswa.2022.117297.
URL <https://www.sciencedirect.com/science/article/pii/S0957417422006625>

- [29] Y. Qin, J. Zhou, D. Chen, [Unsupervised Health Indicator Construction by a Novel Degradation-Trend-Constrained Variational Autoencoder and Its Applications](#), IEEE/ASME Transactions on Mechatronics 27 (3) (2022) 1447–1456. doi:10.1109/TMECH.2021.3098737.
URL <https://ieeexplore.ieee.org/abstract/document/9492834>
- [30] G. Frusque, I. Nejjar, M. Nabavi, O. Fink, [Semisupervised Health Index Monitoring With Feature Generation and Fusion](#), IEEE Transactions on Reliability (2024) 1–15doi:10.1109/TR.2024.3496076.
URL <https://ieeexplore.ieee.org/document/10769583/>
- [31] L. Biggio, T. Bendinelli, C. Kulkarni, O. Fink, [Ageing-aware battery discharge prediction with deep learning](#), Applied Energy 346 (2023) 121229. doi:10.1016/j.apenergy.2023.121229.
URL <https://www.sciencedirect.com/science/article/pii/S0306261923005937>
- [32] S. Pepe, J. Liu, E. Quattrocchi, F. Ciucci, [Neural ordinary differential equations and recurrent neural networks for predicting the state of health of batteries](#), Journal of Energy Storage 50 (2022) 104209. doi:10.1016/j.est.2022.104209.
URL <https://www.sciencedirect.com/science/article/pii/S2352152X22002407>
- [33] Z. Zhou, T. Li, Z. Zhao, C. Sun, X. Chen, R. Yan, J. Jia, [Time-varying trajectory modeling via dynamic governing network for remaining useful life prediction](#), Mechanical Systems and Signal Processing 182 (2023) 109610. doi:10.1016/j.ymssp.2022.109610.
URL <https://www.sciencedirect.com/science/article/pii/S0888327022007002>
- [34] R. T. Q. Chen, Y. Rubanova, J. Bettencourt, D. K. Duvenaud, [Neural Ordinary Differential Equations](#), in: Advances in Neural Information Processing Systems, Vol. 31, Curran Associates, Inc., 2018.
URL https://proceedings.neurips.cc/paper_files/paper/2018/hash/69386f6bb1dfed68692a24c8686939b9-Abstract.html
- [35] Y. Rubanova, R. T. Q. Chen, D. Duvenaud, [Latent ODEs for Irregularly-Sampled Time Series](#), arXiv:1907.03907 (Jul. 2019).
URL <http://arxiv.org/abs/1907.03907>

- [36] J. Morrill, C. Salvi, P. Kidger, J. Foster, T. Lyons, [Neural Rough Differential Equations for Long Time Series](#), arXiv:2009.08295 [cs] (Jun. 2021). doi:10.48550/arXiv.2009.08295.
URL <http://arxiv.org/abs/2009.08295>
- [37] S. I. Holt, Z. Qian, M. v. d. Schaar, [Neural Laplace: Learning diverse classes of differential equations in the Laplace domain](#), in: Proceedings of the 39th International Conference on Machine Learning, PMLR, 2022, pp. 8811–8832, iSSN: 2640-3498.
URL <https://proceedings.mlr.press/v162/holt22a.html>
- [38] N. H. Nguyen, T. M. Nguyen, Improving Neural Ordinary Differential Equations with Nesterov’s Accelerated Gradient Method (2022).
- [39] M. Caldana, J. S. Hesthaven, [Neural Ordinary Differential Equations for Model Order Reduction of Stiff Systems](#), arXiv:2408.06073 (Aug. 2024).
URL <http://arxiv.org/abs/2408.06073>
- [40] T. Qiu, [Multi-Scale Modeling of Financial Systems Using Neural Differential Equations: Applications to High-Frequency Trading, Regime Switching, and Portfolio Optimization](#), 2025.
URL <https://openreview.net/forum?id=9niAAZES5o>
- [41] P. Kokotovi?, H. K. Khalil, J. O’Reilly, [Singular Perturbation Methods in Control: Analysis and Design](#), Classics in Applied Mathematics, Society for Industrial and Applied Mathematics, 1999. doi:10.1137/1.9781611971118.
URL <https://epubs.siam.org/doi/book/10.1137/1.9781611971118>
- [42] M. A. Chao, C. Kulkarni, K. Goebel, O. Fink, [Aircraft Engine Run-to-Failure Dataset under Real Flight Conditions for Prognostics and Diagnostics](#), Data 2021, Vol. 6, Page 5 6 (1) (2021) 5, publisher: Multidisciplinary Digital Publishing Institute. doi:10.3390/DATA6010005.
URL <https://www.mdpi.com/2306-5729/6/1/5/htm>
- [43] I. Loshchilov, F. Hutter, [Decoupled Weight Decay Regularization](#), arXiv:1711.05101 [cs] (Jan. 2019). doi:10.48550/arXiv.1711.05101.
URL <http://arxiv.org/abs/1711.05101>

- [44] A. Paszke, S. Gross, F. Massa, A. Lerer, J. Bradbury, G. Chanan, T. Killeen, Z. Lin, N. Gimelshein, L. Antiga, others, Pytorch: An imperative style, high-performance deep learning library, Advances in neural information processing systems 32 (2019).
- [45] M. Z. Sarwar, D. Cantero, [Probabilistic autoencoder-based bridge damage assessment using train-induced responses](#), Mechanical Systems and Signal Processing 208 (2024) 111046. doi:10.1016/j.ymssp.2023.111046.
URL <https://linkinghub.elsevier.com/retrieve/pii/S0888327023009548>
- [46] S. Massaroli, M. Poli, J. Park, A. Yamashita, H. Asama, [Dissecting Neural ODEs](#), in: Advances in Neural Information Processing Systems, Vol. 33, Curran Associates, Inc., 2020, pp. 3952–3963.
URL <https://proceedings.neurips.cc/paper/2020/hash/293835c2cc75b585649498ee74b395f5-Abstract.html>